Cryo-EM visualization of intermolecular pi-electron interactions within pi-conjugated peptidic supramolecular polymers

Shane T. Rich-New[1,#], Runlai Wang[2,#], Ayisha Zia[1], Fengbin Wang[1,*], John D. Tovar[2,3,*]

Affiliations:

1) Department of Biochemistry and Molecular Genetics, University of Alabama at Birmingham, Birmingham, AL 35233, USA

2) Department of Chemistry, Johns Hopkins University, Baltimore, MD 21218, USA

3) Department of Materials Science and Engineering, Johns Hopkins University, Baltimore, MD 21218, USA

*Correspondence: jerrywang@uab.edu, tovar@jhu.edu

[#]These authors contributed equally

Keywords: cryo-EM, pi-peptide, helical filament, self-assembly, pi-stacking, polymorphism, nanofibers

ABSTRACT

The self-assembly of “pi-peptides” – molecules with pi-electron cores substituted with two or more oligopeptide chains – brings organic electronic function into biologically relevant nanomaterials. Pi-peptides assemble into fibrillar nanomaterials as driven by enthalpic peptide-based hydrogen bonding networks and pi-core-based quadrupolar interactions. A large body of spectroscopic, morphological and computational studies informs on the nature of the self-assembly process and the resulting nanostructures, but detailed structural information has remained elusive. Inspired by the recent use of cryogenic Electron Microscopy (cryo-EM) to provide high-resolution structures for synthetic peptide nanomaterials, we present here the use of cryo-EM to offer ca. 3 Å resolution of pi-peptide nanomaterial assemblies, visualizing for the first time the nature of the intermolecular pi-core electronic interactions responsible for energy transport through these supramolecular materials.

TOC/Abstract Graphic

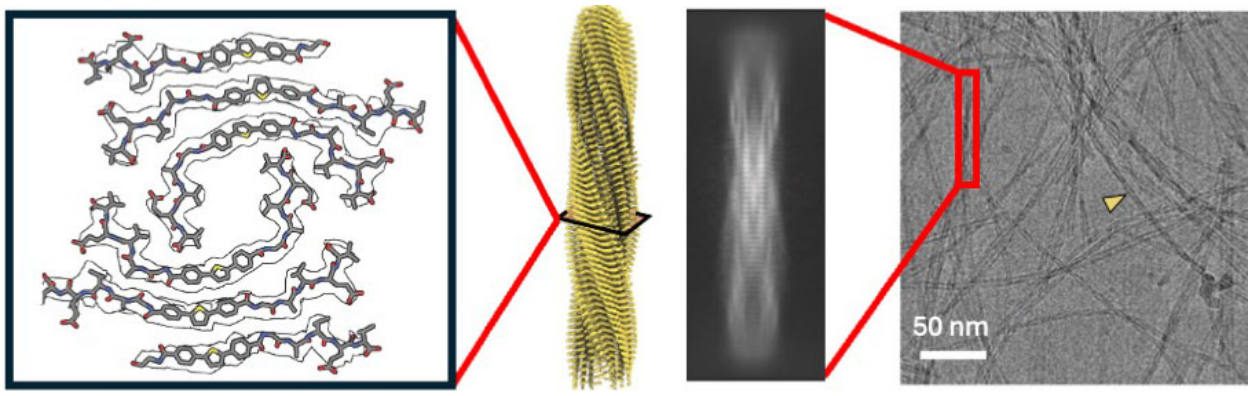

INTRODUCTION

The elucidation of structure–property relationships in supramolecular assemblies is pivotal for advancing molecular design and functional material development[1, 2], yet direct structural visualization remains as a major challenge[3]. For example, energy flow through biological assemblies plays a critical role in processes as diverse as photosynthesis and DNA damage. Spectroscopic interrogation of the key chromophores involved along with atomistic structural insight concerning their disposition in space are key to understanding or perhaps manipulating these energy transfer events. These approaches are equally important to understanding energy migration within abiotic pi-conjugated organic electronic materials that similarly depend on precise interactions of pi-electron quadrupole moments in order to guide carrier migration or recombination. Traditional characterization techniques, including X-ray crystallography, small-angle X-ray scattering (SAXS), nuclear magnetic resonance (NMR) spectroscopy, atomic force microscopy (AFM), scanning electron microscopy (SEM), and transmission electron microscopy (TEM), have provided valuable insights into these structures and have also been augmented by high-level computational simulations. However, each experimental method presents limitations: X-ray crystallography sometimes reaches atomic resolution but requires building blocks to be packed into crystals with a space group, which is almost always incompatible with the symmetry of helical polymers in soft materials; SAXS and NMR can yield ensemble-averaged structural information in solution but lack the spatial resolution needed to resolve nanoscale features or packing arrangements[4]; AFM, SEM and TEM, while offering surface morphology with nanoscale precision, may not accurately reflect native solution-state conformations due to the typical involvement of film preparation and negative staining.

In recent years, cryogenic electron microscopy (cryo-EM) has emerged as a powerful tool in structural biology[5], enabling high-resolution visualization of biomolecular complexes in their near-native states. Despite its success in biology, applications of cryo-EM in supramolecular chemistry remain limited, primarily due to challenges such as the intrinsic heterogeneity, polymorphism, lack of global symmetry, and difficulties in indexing the helical symmetries of synthetic materials[6-12]. Notwithstanding these barriers, cryo-EM

offers a unique opportunity to directly image self-assembled nanostructures with high spatial resolution, without the need for crystallization or staining, making it particularly attractive for characterizing dynamic or polymorphic systems. In fact, this technique has recently been employed to resolve controversies regarding the nature of electrical conduction of bacterial appendage which was found to be mediated in part by closely stacked heme molecules in cytochrome proteins[13].

Peptides are versatile substituents able to influence pi-electron interactions within amyloid-like self-assembled materials. Our group developed several “pi-peptides” whereby a variety of central pi-electron cores reminiscent of standard organic electronic materials were substituted with 2 (or more) oligopeptide sequences about the pi-core periphery[14-16]. These molecules are driven to self-associate by way of the emerging hydrogen-bonding networks that also carry the associated pi-cores into electronically coupled architectures. Using sequence variation, we demonstrated a wide variety of optoelectronic attenuation such as control of excimer formation[17], control of energy transfer[18] and control of chiroptical properties[19], primarily as determined via spectroscopic interrogation and quantum chemical calculations. Many of the underlying structural origins of these attenuations have been elucidated in part through careful modeling studies using atomistic molecular dynamics simulations and course-grained methods[20]. Unlike other traditional electronic materials, we have so far been unable to achieve experimental atomistic resolution of the intermolecular pi-electron interactions which determine the photophysical or electrical outcomes of the energy transport. Scattering data and solid-state NMR spectroscopy have revealed key intermolecular distances, indicating a pi-pi stacking distance of ca 4.6-5.0 Å[21, 22]. Further structural refinement will be necessary not only to corroborate spectroscopic observables or to predict new targets that may possess a desired intermolecular pi-electron geometric relation. In this work, we demonstrate how cryo-EM is able to provide such atomistic detail at ca. 3 Å resolution.

RESULTS AND DISCUSSION

Pi-conjugated cores substituted with peptide sequences containing VEVAG form soluble pi-peptide conjugates that can be driven to self-assemble into amyloid-like fibrils upon changes in solution pH. Furthermore, variations the pi-core electronic structure and the alkyl spacer length between the peptide and the pi-core are known to strongly influence the chemical and physical properties of these materials[19]. Pi-peptides **1** and **2** were designed based on this strategy, both featuring a diphenylthiophene (DPT) central pi-core flanked by VEVAG peptide wings and connected by a spacer which differed only by a single methylene (CH_2) group (Fig. 1). Self-assembled materials from these two pi-peptides displayed similar morphologies under negative staining TEM, but showed significant differences in chiroptical properties as measured by circular dichroism[19] (CD, Fig. 1), which showed inversions in the signs of the bisignate Cotton effects associated with the exciton coupling of the core pi-systems in helical chiral environments. This would ordinarily suggest a change in the macromolecular chirality/helicity within the assembled nanomaterials (e.g. a switch from a right- to left-handed helical twist). To further elucidate the molecular basis of these differences, we compared the self-assembled products of these two pi-peptide conjugates using cryo-EM, with the intention of elucidating the molecular basis of the chirality switch through direct structural visualization. These findings underscore the intricate nature of supramolecular pi-systems and highlight the potential of cryo-EM as a powerful tool for probing the architectures and emergent electronic structures of pi-conjugated soft nanomaterials,

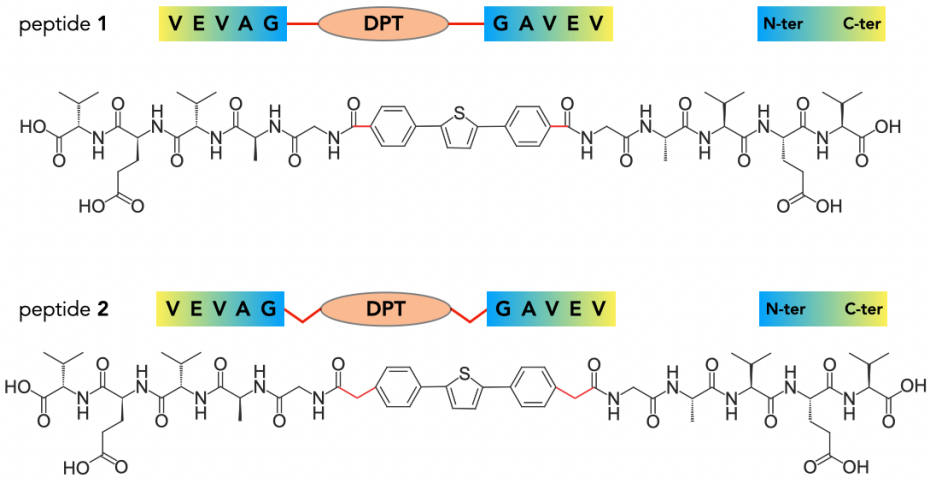

Figure 1 Pi-conjugated peptides synthesized with different methylene (CH_2) spacer lengths between the pi-core and the peptide amides

Cryo-EM of pi-conjugated peptide without spacer

First, we imaged the self-assembly products of peptide **1** under cryo-EM (Fig. 2A). From the reference-free 2D classifications of 5.8 million auto-picked particles, it is clear that there are more than one type of self-assembled nanostructure. Such heterogeneity in the self-assembled products from small peptides is not rare. A few such peptide[23] and small molecule[24, 25] examples, involving strong pi-pi interactions, have been reported by cryo-EM. Among those 5.8 million auto-picked particles, after removing ~1.8 million junk particles such as lacy carbon edges, there is only one dominant nanostructure class, accounting for ~50% of particles left, showing clear high-resolution features (Fig. 1B). Other classes are mostly smeared, displaying different diameter, pitch, morphology, etc., suggesting they are probably self-assembled filamentous products without a consistent repeating architecture along the filament.

The helical symmetry of the peptide **1** nanostructure was determined to be C2, with a helical rise of 4.75 Å and a twist of -4.29°, and a diameter of approximately 6 nm. The final 3D helical reconstruction reached a final resolution of 3.4 Å as judged by the map:map FSC method (Figure S1). The resulting reconstruction shows a clear parallel cross-β packing of peptide **1** and demonstrates that hydrogen bond networks are formed between adjacent peptide subunits along the filament (Fig. 2C). Furthermore, the DPT pi-cores appear to significantly contribute to the supramolecular structure through strong pi-pi stacking along the filament. A cross-sectional view revealed two asymmetrical units (ASUs) related by the C2 symmetry, each containing a trimer of peptide **1**. Three DPTs in the ASU cluster in the middle. One of the conjugated VEVAG is disordered for the peptide copy near the outer surface, presumably due to a lack of interface restraints with other molecules (Fig. 2D). Our prior computational modeling reproduced the pronounced deviation from linearity of the pi-peptides most buried within the nanostructures[26] (e.g. components 3 and 6 in Fig. 2D), including a tendency to further curve up as the pi-core size is increased[27].

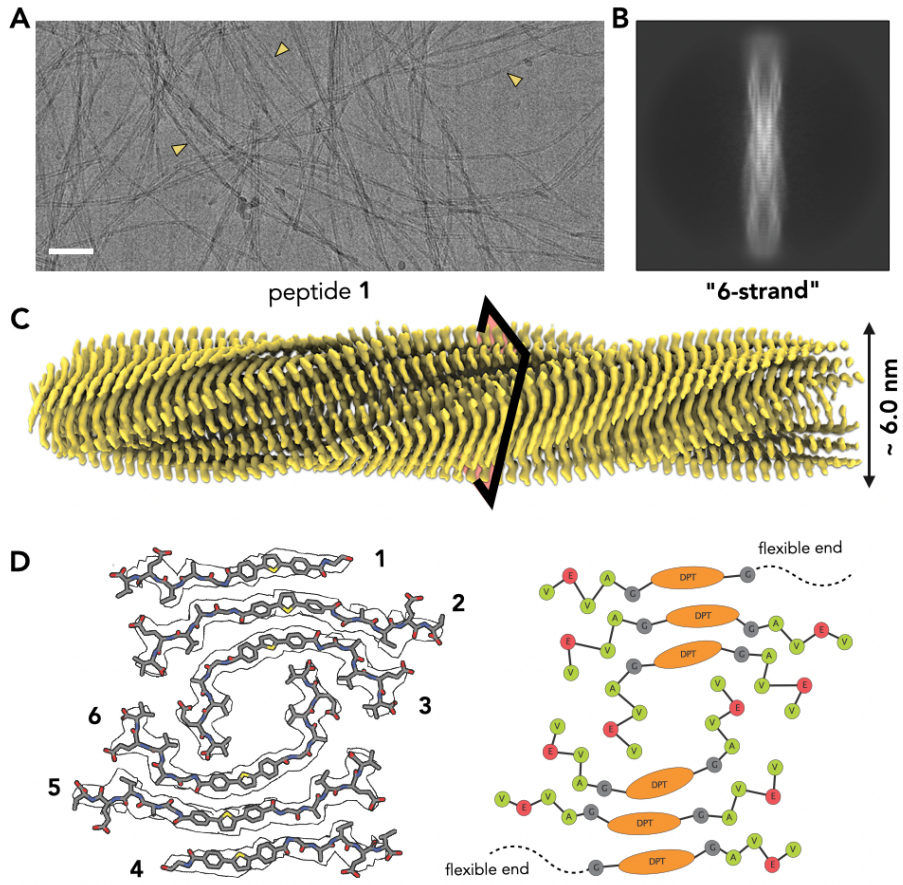

Figure 2 | Cryo-EM of self-assembled nanostructure of peptide 1

(**A**) A representative cryo-EM micrograph shows nanostructures formed by peptide **1** (indicated by yellow arrowheads). Scale bar: 50 nm.

(**B**) A representative 2D average of the peptide **1** nanostructure.

(**C**) 3D helical reconstruction of the nanostructure at near-atomic resolution provides detailed structural information.

(**D**) A cross-section of the nanostructure from (**C**) with an atomic model fitted into the cryo-EM map. The cartoon illustration of the atomic model is shown on the right.

Pi-conjugate morphological heterogeneity results from alkyl spacer addition

Peptide **2**, which differs from peptide **1** by a single additional alkyl group in the spacer connecting the DPT and pentapeptide, exhibited a significantly different circular dichroism (CD) spectrum suggestive of an ensemble change in the macromolecular helicity/chirality. Consequently, we examined peptide **2** using cryo-EM (Fig. 3A). In contrast to the single, dominant ordered morphology observed for peptide **1**, cryo-EM

micrograph and reference-free 2D classification of peptide **2** revealed three distinct species with high-resolution features EM (Fig. 3A-B). These three nanostructure species were easily distinguished based on their diameters and morphologies. The nanostructure diameters were approximately 8 nm, 6.5 nm, and 5.5 nm, representing ~62%, 18%, and 20% of the total nanostructure population, respectively (Fig. 3B). The thinnest 5.5 nm species displayed considerably greater flexibility in the 2D classes compared to the other two, resulting in a low-resolution reconstruction that precluded near-atomic resolution (Figure S2).

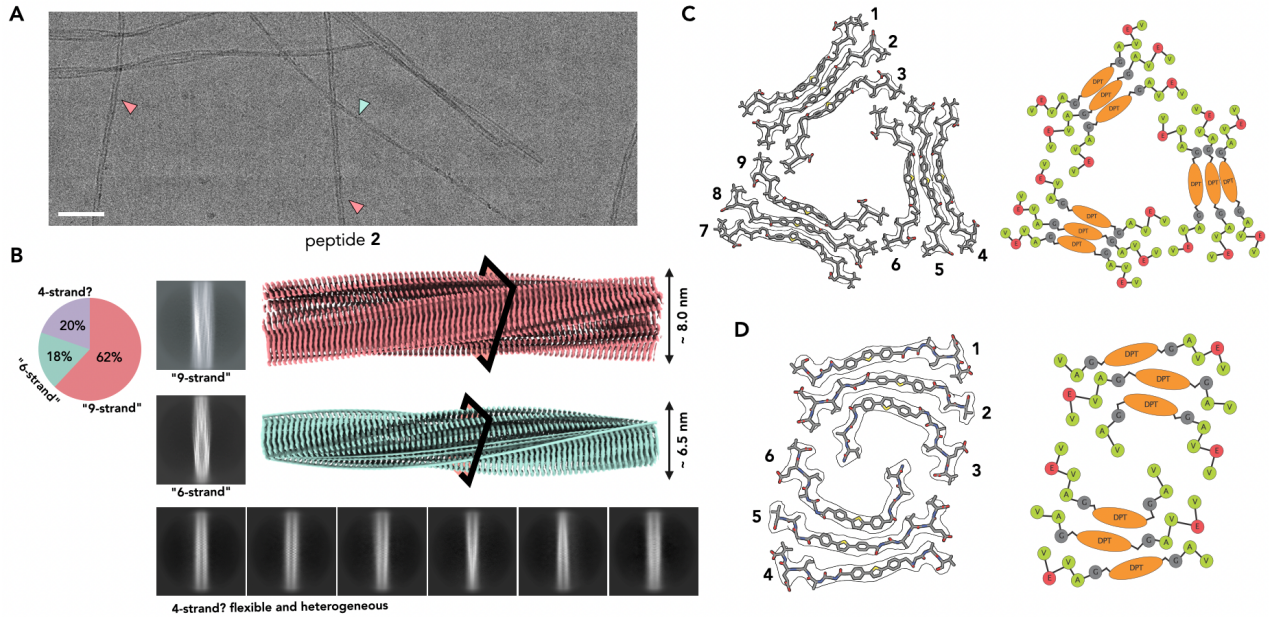

Figure 3 | Cryo-EM of self-assembled nanostructures of peptide 2

(**A**) A representative cryo-EM micrograph shows nanostructures formed by peptide **2**. Nanostructures with different morphologies are indicated by arrowheads with different colors. Scale bar: 50 nm.

(**B**) The relative abundance of the observed nanostructure species, their corresponding 2D averages, and their 3D helical reconstructions. The colors are consistent with the labels in (**A**).

(**C**) A cross-section of the 9-strand nanostructure with an atomic model fitted into the cryo-EM density map. The cartoon illustration of the atomic model is shown on the right.

(**D**) A cross-section of the 6-strand nanostructure with an atomic model fitted into the cryo-EM density map. The cartoon illustration of the atomic model is shown on the right.

In contrast, the cryo-EM reconstructions of the 8 nm and 6.5 nm nanostructures reached resolutions of 2.9 Å and 3.2 Å (Figure S1), respectively. The 8 nm nanostructure of peptide **2** exhibited C1 symmetry, a helical rise of 1.60 Å, and a helical twist of -120.44°. Cross-sectional analysis revealed three asymmetric units (ASUs), each containing three peptide copies, for a total of nine peptide strands per cross-section. Similar to peptide **1**, peptide subunits clustered into trimeric ASUs. However, unlike peptide **1**, which had two ASUs in the cross-section, the 8 nm nanostructure adopted an additional ASU, forming a 3-protofilament architecture (Fig. 3C). The 6.5 nm nanostructure of peptide **2** displayed C1 symmetry, a helical rise of 2.35 Å, and a helical twist of 178.81°. Cross-sectional analysis showed two ASUs, each containing three peptide copies. While the number of peptides per cross-section was similar to peptide **1**, their arrangement in helical symmetries and inter-ASU contacts were significantly different (Fig. 3D). The low-resolution reconstruction of the thinnest 5.5 nm nanostructure species suggested a cross-section containing four peptide copies, lacking the trimeric arrangement within the ASU (Figure S2). This indicates that the trimeric arrangement of peptides forms a more stable and robust core for self-assembly. Alternative nuclei, such as the 4-strand core, is possible, but the resulting products have significantly greater flexibility.

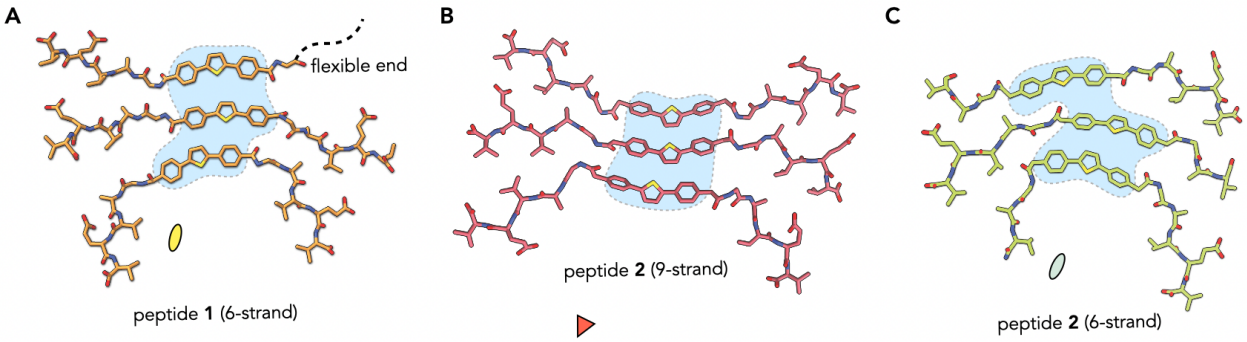

Figure 4 | Nanostructure building blocks.
The asymmetric units of three distinct nanostructures are shown: (**A**) 6-strand peptide **1**; (**B**) 9-strand peptide **2**; and (**C**) 6-strand peptide **2**. The helical axis locations are indicated with ovals for two protofilament structures and triangle for three protofilament structure. The areas of three DPTs are also highlighted.

Peptide 1 vs. Peptide 2

Despite variations in helical symmetries, the ordered nanostructures of peptide **1** and peptide **2** consistently exhibit asymmetric units (ASUs) composed of three peptide subunits. However, the inter-peptide interfaces within these ASUs demonstrate plasticity and are not uniform across the different nanostructures. This variability might not solely come from the additional methylene group; it could also be influenced by the arrangement of the three DPTs within the ASU. For instance, in the ASU of peptide **1**, the top two DPTs are roughly aligned, while the bottom DPT is shifted left by one aromatic ring (Fig. 4A). In contrast, the 9-strand nanofiber of peptide **2** displays all three DPTs aligned within the ASU (Fig. 4B). Conversely, in the 6-strand nanostructure of peptide **2**, the bottom two DPTs maintain a similar orientation to those in the 6-strand nanostructure of peptide **1**, but the top DPT is shifted left by two aromatic rings (Fig. 4C). This shift results in the outer peptide copy within the 6-strand nanostructure of peptide **2** becoming ordered in the architecture.

The interface between peptide subunits across different layers of the ASU along the protofilament is quite similar for peptide **1** and peptide **2**. As anticipated, this interface is formed by both pi-pi interactions within the pi-conjugate core and cross-β hydrogen bonds on both sides of the subunit (Fig. 5A). Specifically, for the pi-pi interactions (Fig. 5B), the plane-to-plane distance in peptide **1** is approximately 4.4 Å. In peptide **2**, this distance ranges from 4.7 to 4.8 Å, which aligns with measurements in other pi-conjugated peptide systems (REF???). Moreover, since the molecules in peptide 1 exhibit a larger tilt angle in their packing arrangement, their ring-to-ring distance is 5.0 Å, slightly greater than the 4.8 Å observed in peptide 2 (Fig. 5C). The hydrogen bonding networks across all nanofibers are consistent with what's expected for cross-β peptide packing (Fig. 5C). While under current resolution (3-4 Å), it's not possible to unambiguously determine precise hydrogen bond lengths, the helical symmetry indicates that these amino acids adopt a β-sheet packing arrangement.

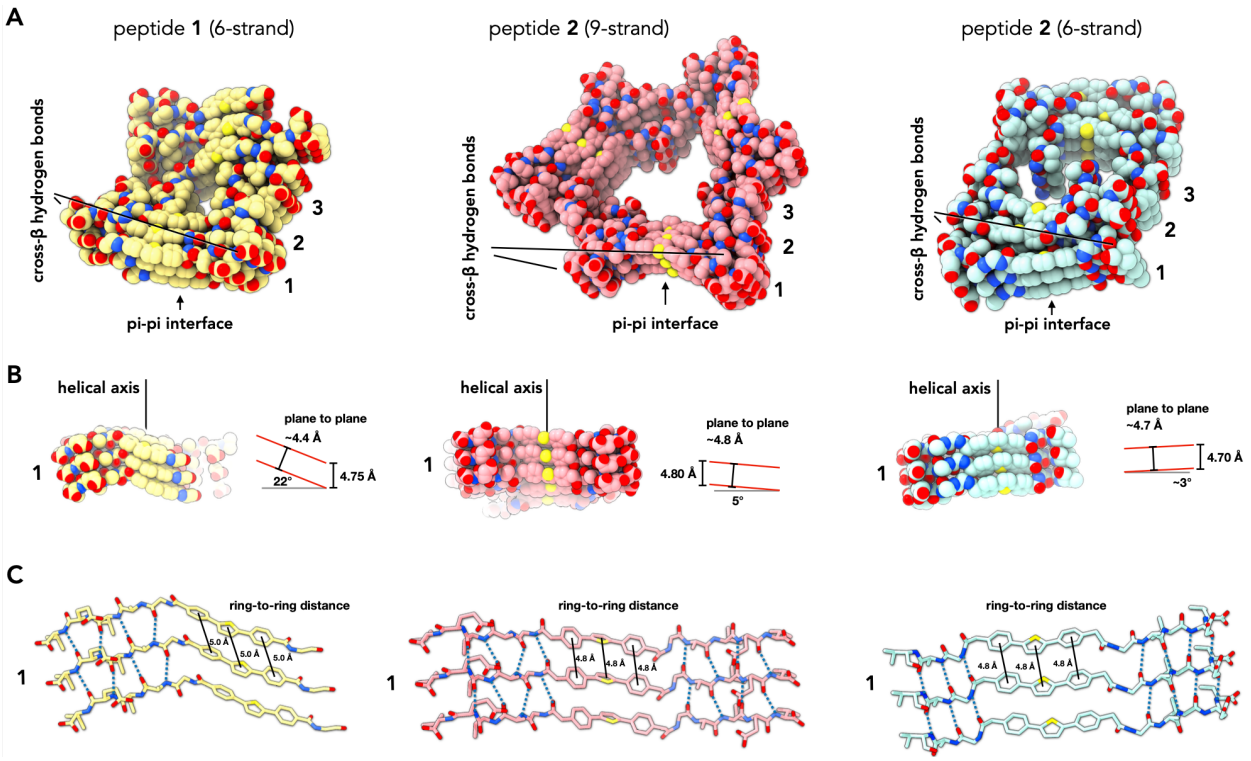

Figure 5 | pi-conjugate interface within protofilament.

The pi-conjugate interface within a single protofilament is analyzed. (**A**) Three layers of pi-conjugates are shown as spheres for peptide **1** and peptide **2**. Three copies of the pi-conjugate within a single ASU are labeled "1," "2," and "3," consistent with previous figures. The areas of the pi-pi interface and hydrogen bonds are indicated. (**B**) Viewing from the outside to visualize the pi-pi interface, the subunit rise along the helical axis, and the plane-to-plane distance are labeled. (**C**) The measured ring-to-ring distance and detected hydrogen bonds for subunit 1 are shown for both peptide **1** and peptide **2**.

Hand of nanostructures and reconcile with previous CD measurements

Analyzing the axial packing within these nanostructures reveals that the cross-β parallel-packed ASUs all adopt a left-handed twist within the protofilament. The rise and twist within a protofilament are 4.75 Å and -4.29° for peptide **1**, 4.8 Å and -1.32° for the 9-strand nanostructure of peptide **2**, and 4.7 Å and -2.38° for the 6-strand nanostructure of peptide **2**, respectively. The differences in twist suggest that the three-subunit ASUs possess significant plasticity, accommodating variable cross-β interfaces. This left-handed twist in such cross-β fibers is consistent with numerous protein/peptide amyloid

structures previously determined[28-31]. Although cryo-EM imaging does not contain the handedness information, our modeling attempts using both chiral forms of cryo-EM maps consistently yielded better hydrogen bonding formation in the left-handed protofilament maps. Therefore, the observed differences in CD measurements for peptide 1 and peptide 2 are not attributable to different protofilament chirality.

Although it is possible in principle to use this structural information in order to extract some optoelectronic properties (such as electronic absorption spectra[32]), in the present case, preliminary calculations suggest that the absorption energies reflecting the inherent torsional twisting of the isolated PTP chromophore coincide ambiguously with bands associated with the pi-peptide as observed experimentally or in calculations of dimer structures based off of the structural data reported here. In solution, there is anticipated free rotation of these bonds which leads to the broad spectral response in the UV-vis absorption (as opposed to one sharp peak for one specific pi-system). As the individual aromatic rings approach more coplanar geometries, the HOMO-LUMO gap energy should decrease on account of enhanced intramolecular conjugation. Within the structural data are different conformations of the pi-cores with dramatically different dihedral angles about the C-C single bonds that connect the aromatic rings in the pi-core, some of which approach planarity and surprisingly, some which are dramatically driven away from planarity. This is likely because, at such a resolution, the cryo-EM map does not provide sufficient information to accurately determine the ring's position. Additionally, it is possible that the rings have some flexibility within the packed assembly. After helical averaging, the resulting density would be an average of these different positions, making the modeling process more challenging. Unfortunately, the calculations just of these isolated molecular extremes provide spectral transitions in the same region as our assigned “molecular” and “H-like aggregates” regardless of any subsequent intermolecular interactions. We therefore cannot conclude whether the calculated spectra correspond to the geometries of the intermolecular pi-stacking or are inherent to the conformations of the molecular precursors which make up the aggregate. Furthermore, the calculation of anticipated circular dichroism outcomes due to the associated macromolecular chirality is still elusive. Given that CD spectroscopy provides a bulk measurement of the average chirality of all components in solution, the differences in CD

measurements between peptide **1** and peptide **2** likely arise from the formation of distinct nanostructure sets and nucleated from different small aggregates with varying intermolecular pi-core orientations in the solution phase. The heterogeneous nature of the self-assembled products complicates the deconvolution of individual nanostructure species' contributions from the CD spectrum.

CONCLUSIONS

In this study, we present for the first time high resolution structural details of self-assembled nanomaterials derived from pi-peptide assembly as extracted with cryo-EM, in many cases achieving ca. 3 Å resolution. Previous speculations regarding the similarity of the assembly processes of traditional amyloidogenic peptides and these artificial pi-peptides, which were loosely founded upon inspection of spectroscopic data and transmission electron microscopy, are now affirmed with much higher resolution and atomistic detail. Unlike related imaging accomplished for other types of protein-based nanomaterials, the structures here reveal critical geometric information related to the disposition of optoelectronically relevant pi-core groups within the aggregates, whose spatial orientations and interactions through space play direct roles in the subsequent energy transfer processes operative or possible. We expect that these structural insights will prove useful for refining future computational modeling studies on these nanomaterials as well as for validating our current efforts to achieve predictive insight on how peptide sequence and pi-core variations in these pi-peptides can lead to attenuated optoelectronic and energy migration outcomes within these nanoscale assemblies.

METHODS

Pi-peptide hydrogel formation.

Pi-peptide **1** and pi-peptide **2** were prepared according to prior reports[19]. These pi-peptides were self-assembled using an identical protocol. First, a 1 mg/mL aqueous solution of each conjugated peptide was prepared and gently mixed by pipetting to ensure complete dissolution. Then, 100 µL of this solution was transferred to a glass vial. An HCl vapor chamber was prepared by placing another glass vial containing concentrated HCl (12 N) inside a larger, capped glass jar. The HCl vapor was allowed to diffuse for 5 minutes before the peptide solution vial was placed inside. The peptide solution was incubated in this chamber for 5 minutes to allow the assembly process to initiate and complete. Gelation of the solution was observed for both peptides. The gel sample was diluted 30- to 100-fold with water prior to cryo-EM analysis.

Cryo-EM of pi-conjugated peptide nanostructures.

Each peptide hydrogel sample (4.5 µL) was applied to glow-discharged lacey carbon grids and then plunge-frozen using a Leica EM GP2 plunge freezer. Imaging was performed on a 300 keV Titan Krios equipped with a Gatan K3 direct electron detector camera in counting mode, with a total dose of 50 $e^-/Å^2$. The pixel sizes used for peptide 1 and peptide 2 were 1.12 Å per pixel and 1.09 Å per pixel, respectively. The cryo-EM workflow began with patch motion correction[33] and CTF estimation in cryoSPARC[34]. Following these steps, "Filament Tracer," an automated segment picking tool, was used to pick particles with a 10 Å shift between adjacent segment picks. The resulting particles were subjected to several iterations of 2D classification, selecting classes with high-resolution features for each subsequent round, and removing all "bad" particles, such as those at carbon edges or blurred, low-resolution classes. Next, possible helical symmetries were calculated from averaged power spectra generated from aligned raw particles[35]. Each possible symmetry (helical rise, twist, and point group symmetry) was tested using "Helix Refine" by trial and error until recognizable peptide and pi-conjugate features were visible[36]. After determining the correct symmetry, a local CTF refinement was performed, and the CTF-refined particles were used for another round of "Helix

Refine". The final reconstruction was sharpened using EMReady, and helical symmetry was re-applied using himpose[37] within the SPIDER[38] package.

Model building of pi-conjugated peptide nanostructures

Because these nanostructures contain predominantly β-sheets, the handedness of the cryo-EM maps could not be determined directly from the maps themselves[36]. Therefore, we built the model into both hands of the map, and in all cases, we observed that the model built into the left-handed protofilaments had a better overall real-space correlation coefficient (RSCC) and more hydrogen bonds between β-sheets. The model-building process was more complicated than traditional modeling due to the presence of a non-standard aromatic DPT molecule in the center and a pentapeptide on each side of a DPT molecule, with the N-terminus of each pentapeptide conjugated to the DPT. Specifically, to accurately place DPTs into the map, we first defined the entire pi-conjugated peptide as a single ligand compound using eLBOW[39]. We then manually refined the peptide into the map in Coot[40] and subsequently performed real-space refinement in PHENIX[41]. The placement of the entire molecule was guided not only by the DPT shape but also by the clearly observed densities of peptide side chains. Afterward, the placement of DPT was relatively accurate, but the peptide portion had not been refined using known peptide geometry constraints, such as the Ramachandran plot. Therefore, we re-defined the central DPT region (including the methylene group in peptide **2**) as a ligand compound, maintained its real-space-refined position, and converted the peptide portion into a canonical peptide format. This molecule was then subjected to another round of real-space refinement in PHENIX[41]. The cryo-EM parameters and model refinement statistics for the peptide nanostructures are shown in Table 1.

Table 1 Cryo-EM data collection and refinement statistics

Parameters	Peptide 1	Peptide 2 (9 strands)	Peptide 2 (6 strands)
Data collection and processing			
Voltage (kV)	300	300	300
Electron exposure (e^{-} Å^{-2})	50	50	50
Pixel size (Å)	1.12	1.09	1.09
Particle images (n)	304,634	2,342,281	488,485
Shift (pixel)	10	40	40
Helical symmetry			
Point group	C2	C1	C1
Helical rise (Å)	4.75	1.60	2.35
Helical twist (°)	-4.29	-120.44	178.81
Resolution estimation (Å)			
Map:map FSC (0.143)	3.4	2.9	3.2
Model:map FSC (0.5)	3.6	3.5	4.1
Refinement and Model validation			
Clashscore	9.9	58.4	35.1
Ramachandran Favored (%)	98.5	100.0	100.0
RSCC	0.74	0.86	0.81
Deposition ID			
PDB (model)	9O7J	9O7K	9O7L
EMDB (map)	EMD-70201	EMD-70202	EMD-70203

Supporting information available

wwPDB EM validation results, calculations, analysis of a putative 4-strand assembly.

Data availability

The three-dimensional reconstructions of peptide **1** and peptide **2** nanostructures have been deposited in the Electron Microscopy Data Bank with accession codes EMD-70201, EMD-70202, and EMD-70203. The corresponding atomic models have been deposited in the Protein Data Bank with accession code 9O7J, 9O7K, and 9O7L.

Acknowledgments

This research was, in part, supported by the National Cancer Institute's National Cryo-EM Facility at the Frederick National Laboratory for Cancer Research under contract 75N91019D00024. Electron microscopy screening was carried out in the UAB Cryo-EM Facility, supported by the Institutional Research Core Program and O'Neal Comprehensive Cancer Center (NIH grant P30 CA013148), with additional funding from NIH grant S10 OD024978. We are grateful to Dr. James Kizziah, Dr. Adam Wier and Dr. Tara Fox for assisting with the screening or data collection. We thank Prof. Miklos Kertesz (Georgetown University) for helpful discussions regarding electronic absorption calculations. The work in F.W. laboratory was supported by NIH grant GM138756 and DE-SC0024303. The work in J.D.T. laboratory was supported by Johns Hopkins University and NSF grant 1728947.

Author contributions

R. W. synthesized the conjugated pi-peptides. S.T.R. and R. W. performed the peptide self-assembling experiments. S.T.R. performed cryo-EM and data analysis. S.T.R. and A.Z. did the peptide modeling. F.W. and J.D.T. supervised the research and obtained funding. S.T.R., R. W., F.W. and J.D.T. wrote the manuscript with input from all authors.

Competing interests

The authors declare no competing interests.

References

(1) Aida, T.; Meijer, E. W.; Stupp, S. I. Functional supramolecular polymers. *Science* **2012**, *335* (6070), 813-817. DOI: 10.1126/science.1205962 From NLM Medline.

(2) Busseron, E.; Ruff, Y.; Moulin, E.; Giuseppone, N. Supramolecular self-assemblies as functional nanomaterials. *Nanoscale* **2013**, *5* (16), 7098-7140, 10.1039/C3NR02176A. DOI: 10.1039/C3NR02176A.

(3) Venugopal, A.; Ruiz-Perez, L.; Swamynathan, K.; Kulkarni, C.; Calò, A.; Kumar, M. Caught in Action: Visualizing Dynamic Nanostructures Within Supramolecular Systems Chemistry. *Angewandte Chemie International Edition* **2023**, *62* (8), e202208681. DOI: https://doi.org/10.1002/anie.202208681 (acccessed 2025/04/13).

(4) Mertens, H. D. T.; Svergun, D. I. Combining NMR and small angle X-ray scattering for the study of biomolecular structure and dynamics. *Archives of Biochemistry and Biophysics* **2017**, *628*, 33-41. DOI: https://doi.org/10.1016/j.abb.2017.05.005.

(5) Cheng, Y. Single-Particle Cryo-EM at Crystallographic Resolution. *Cell* **2015**, *161* (3), 450-457. DOI: 10.1016/j.cell.2015.03.049 (acccessed 2025/04/13).

(6) Sonani, R.; Bianco, S.; Kreutzberger, M.; Adams, D.; Egelman, E. Cryo-EM for atomic characterization of supramolecular gels. *Faraday Discussions* **2024**, 10.1039/D4FD00181H. DOI: 10.1039/D4FD00181H.

(7) Hughes, S. A.; Wang, F.; Wang, S.; Kreutzberger, M. A. B.; Osinski, T.; Orlova, A.; Wall, J. S.; Zuo, X.; Egelman, E. H.; Conticello, V. P. Ambidextrous helical nanotubes from self-assembly of designed helical hairpin motifs. *Proc Natl Acad Sci U S A* **2019**, *116* (29), 14456-14464. DOI: 10.1073/pnas.1903910116.

(8) Wang, F.; Gnewou, O.; Modlin, C.; Beltran, L. C.; Xu, C.; Su, Z.; Juneja, P.; Grigoryan, G.; Egelman, E. H.; Conticello, V. P. Structural analysis of cross alpha-helical nanotubes provides insight into the designability of filamentous peptide nanomaterials. *Nat Commun* **2021**, *12* (1), 407. DOI: 10.1038/s41467-020-20689-w.

(9) Yi, M.; Wang, F.; Tan, W.; Hsieh, J. T.; Egelman, E. H.; Xu, B. Enzyme Responsive Rigid-Rod Aromatics Target "Undruggable" Phosphatases to Kill Cancer Cells in a Mimetic Bone Microenvironment. *J Am Chem Soc* **2022**, *144* (29), 13055-13059. DOI: 10.1021/jacs.2c05491.

(10) Yu, S.; Ye, Z.; Roy, R.; Sonani, R. R.; Pramudya, I.; Xian, S.; Xiang, Y.; Liu, G.; Flores, B.; Nativ-Roth, E.; et al. Glucose-Triggered Gelation of Supramolecular Peptide Nanocoils with Glucose-Binding Motifs. *Adv Mater* **2024**, *36* (16), e2311498. DOI: 10.1002/adma.202311498 From NLM Medline.
(11) Bigo-Simon, A.; Estrozi, L. F.; Chaumont, A.; Schurhammer, R.; Schoehn, G.; Combet, J.; Schmutz, M.; Schaaf, P.; Jierry, L. 3D Cryo-Electron Microscopy Reveals the Structure of a 3-Fluorenylmethyloxycarbonyl Zipper Motif Ensuring the Self-Assembly of Tripeptide Nanofibers. *ACS Nano* **2024**, *18* (44), 30448-30462. DOI: 10.1021/acsnano.4c08043 From NLM Medline.
(12) Yu, L. T.; Hancu, M. C.; Kreutzberger, M. A. B.; Henrickson, A.; Demeler, B.; Egelman, E. H.; Hartgerink, J. D. Hollow Octadecameric Self-Assembly of Collagen-like Peptides. *Journal of the American Chemical Society* **2023**. DOI: 10.1021/jacs.2c12931.
(13) Wang, F.; Gu, Y.; O'Brien, J. P.; Yi, S. M.; Yalcin, S. E.; Srikanth, V.; Shen, C.; Vu, D.; Ing, N. L.; Hochbaum, A. I.; et al. Structure of Microbial Nanowires Reveals Stacked Hemes that Transport Electrons over Micrometers. *Cell* **2019**, *177* (2), 361-369 e310. DOI: 10.1016/j.cell.2019.03.029.
(14) Tovar, J. D. Supramolecular Construction of Optoelectronic Biomaterials. *Accounts of Chemical Research* **2013**, *46* (7), 1527-1537. DOI: 10.1021/ar3002969.
(15) Vadehra, G. S.; Wall, B. D.; Diegelmann, S. R.; Tovar, J. D. On-resin dimerization incorporates a diverse array of π-conjugated functionality within aqueous self-assembling peptide backbones. *Chem. Commun.* **2010**, *46* (22), 3947-3949, 10.1039/C0CC00301H. DOI: 10.1039/C0CC00301H.
(16) Diegelmann, S. R.; Gorham, J. M.; Tovar, J. D. One-Dimensional Optoelectronic Nanostructures Derived from the Aqueous Self-Assembly of π-Conjugated Oligopeptides. *Journal of the American Chemical Society* **2008**, *130* (42), 13840-13841. DOI: 10.1021/ja805491d.
(17) Wall, B. D.; Zacca, A. E.; Sanders, A. M.; Wilson, W. L.; Ferguson, A. L.; Tovar, J. D. Supramolecular Polymorphism: Tunable Electronic Interactions within π-Conjugated Peptide Nanostructures Dictated by Primary Amino Acid Sequence. *Langmuir* **2014**, *30* (20), 5946-5956. DOI: 10.1021/la500222y.

(18) Honick, C. R.; Panda, S. S.; O'Connor, L. R.; Tovar, J. D.; Bragg, A. E. Supramolecular Tuning of Exciton Transport in Pi-Peptide Assemblies. *The Journal of Physical Chemistry C* **2023**, *127* (3), 1310-1319. DOI: 10.1021/acs.jpcc.2c07014.
(19) Panda, S. S.; Shmilovich, K.; Ferguson, A. L.; Tovar, J. D. Controlling Supramolecular Chirality in Peptide-π-Peptide Networks by Variation of the Alkyl Spacer Length. *Langmuir* **2019**, *35* (43), 14060-14073. DOI: 10.1021/acs.langmuir.9b02683.
(20) Ferguson, A. L.; Tovar, J. D. Evolution of pi-Peptide Self-Assembly: From Understanding to Prediction and Control. *Langmuir* **2022**, *38* (50), 15463-15475. DOI: 10.1021/acs.langmuir.2c02399 From NLM Medline.
(21) Ardona, H. A. M. Molecular Engineering Strategies for the development of energy-transporting conjugated systems towards bioelectronics. Johns Hopkins University, 2017. http://jhir.library.jhu.edu/handle/1774.2/60201.
(22) Wall, B. D. Synthesis and characterization of self-assembling peptides bearing pi-conjugated subunits to study pi-pi interactions. Ph.D., The Johns Hopkins University, United States -- Maryland, 2013.
(23) Guo, J. Q.; Wang, F. B.; Huang, Y. M.; He, H. J.; Tan, W. Y.; Yi, M. H.; Egelman, E. H.; Xu, B. Cell spheroid creation by transcytotic intercellular gelation. *Nature Nanotechnology* **2023**, *18* (9). DOI: 10.1038/s41565-023-01401-7.
(24) Zia, A.; Yi, M. H.; Liu, Z. Y.; Wang, F. B.; Xu, B. Fragment-Based Approach for Hierarchical Nanotube Assembly of Small Molecules in Aqueous Phase. *Chem-Eur J* **2025**. DOI: 10.1002/chem.202404630.
(25) Hall, G. E. K.; Lee, T.; Tovar, J. D.; Katz, H. E. Utilizing pi-peptide supramolecular polymers to template growth of hybrid organic–inorganic electronic materials††Electronic supplementary information (ESI) available. See DOI: https://doi.org/10.1039/d4lf00087k. *RSC Applied Interfaces* **2024**, *1* (5), 944-957. DOI: https://doi.org/10.1039/d4lf00087k.
(26) Thurston, B. A.; D., T. J.; and Ferguson, A. L. Thermodynamics, morphology, and kinetics of early-stage self-assembly of π-conjugated oligopeptides. *Molecular Simulation* **2016**, *42* (12), 955-975. DOI: 10.1080/08927022.2015.1125997.
(27) Jira, E. R.; Shmilovich, K.; Kale, T. S.; Ferguson, A.; Tovar, J. D.; Schroeder, C. M. Effect of Core Oligomer Length on the Phase Behavior and Assembly of π-Conjugated

Peptides. *ACS Applied Materials & Interfaces* **2020**, *12* (18), 20722-20732. DOI: 10.1021/acsami.0c02095.
(28) Yang, Y.; Arseni, D.; Zhang, W.; Huang, M.; Lovestam, S.; Schweighauser, M.; Kotecha, A.; Murzin, A. G.; Peak-Chew, S. Y.; Macdonald, J.; et al. Cryo-EM structures of amyloid-beta 42 filaments from human brains. *Science* **2022**, *375* (6577), 167-172. DOI: 10.1126/science.abm7285 From NLM Medline.
(29) Das, A.; Gnewou, O.; Zuo, X.; Wang, F.; Conticello, V. P. Surfactant-like peptide gels are based on cross-β amyloid fibrils. *Faraday Discussions* **2025**, 10.1039/D4FD00190G. DOI: 10.1039/D4FD00190G.
(30) Qiao, Y. C.; Zia, A.; Wu, G. C.; Liu, Z. Y.; Guo, J. Q.; Chu, M. T.; He, H. J.; Wang, F. B.; Xu, B. Context-Dependent Heterotypic Assemblies of Intrinsically Disordered Peptides. *Journal of the American Chemical Society* **2025**, *147* (4), 2978-2983. DOI: 10.1021/jacs.4c12150.
(31) Fernandez, A.; Hoq, M. R.; Hallinan, G. I.; Li, D.; Bharath, S. R.; Vago, F. S.; Zhang, X.; Ozcan, K. A.; Newell, K. L.; Garringer, H. J.; et al. Cryo-EM structures of amyloid-beta and tau filaments in Down syndrome. *Nat Struct Mol Biol* **2024**, *31* (6), 903-909. DOI: 10.1038/s41594-024-01252-3 From NLM Medline.
(32) Thurston, B. A.; Shapera, E. P.; Tovar, J. D.; Schleife, A.; Ferguson, A. L. Revealing the Sequence-Structure–Electronic Property Relation of Self-Assembling π-Conjugated Oligopeptides by Molecular and Quantum Mechanical Modeling. *Langmuir* **2019**, *35* (47), 15221-15231. DOI: 10.1021/acs.langmuir.9b02593.
(33) Zheng, S. Q.; Palovcak, E.; Armache, J. P.; Verba, K. A.; Cheng, Y.; Agard, D. A. MotionCor2: anisotropic correction of beam-induced motion for improved cryo-electron microscopy. *Nat Methods* **2017**, *14* (4), 331-332. DOI: 10.1038/nmeth.4193.
(34) Rohou, A.; Grigorieff, N. CTFFIND4: Fast and accurate defocus estimation from electron micrographs. *J Struct Biol* **2015**, *192* (2), 216-221. DOI: 10.1016/j.jsb.2015.08.008.
(35) Stewart, M. Computer image processing of electron micrographs of biological structures with helical symmetry. *J Electron Microsc Tech* **1988**, *9* (4), 325-358. DOI: 10.1002/jemt.1060090404 From NLM Medline.

(36) Wang, F.; Gnewou, O.; Solemanifar, A.; Conticello, V. P.; Egelman, E. H. Cryo-EM of Helical Polymers. *Chem Rev* **2022**, *122* (17), 14055-14065. DOI: 10.1021/acs.chemrev.1c00753.
(37) Egelman, E. H. Reconstruction of helical filaments and tubes. *Methods Enzymol* **2010**, *482*, 167-183. DOI: 10.1016/S0076-6879(10)82006-3.
(38) Shaikh, T. R.; Gao, H. X.; Baxter, W. T.; Asturias, F. J.; Boisset, N.; Leith, A.; Frank, J. SPIDER image processing for single-particle reconstruction of biological macromolecules from electron micrographs. *Nat Protoc* **2008**, *3* (12), 1941-1974. DOI: 10.1038/nprot.2008.156.
(39) Moriarty, N. W.; Grosse-Kunstleve, R. W.; Adams, P. D. electronic Ligand Builder and Optimization Workbench (eLBOW): a tool for ligand coordinate and restraint generation. *Acta Crystallogr D Biol Crystallogr* **2009**, *65* (Pt 10), 1074-1080. DOI: 10.1107/S0907444909029436.
(40) Emsley, P.; Cowtan, K. Coot: model-building tools for molecular graphics. *Acta Crystallogr D Biol Crystallogr* **2004**, *60* (Pt 12 Pt 1), 2126-2132. DOI: 10.1107/S0907444904019158.
(41) Afonine, P. V.; Poon, B. K.; Read, R. J.; Sobolev, O. V.; Terwilliger, T. C.; Urzhumtsev, A.; Adams, P. D. Real-space refinement in PHENIX for cryo-EM and crystallography. *Acta Crystallogr D Struct Biol* **2018**, *74* (Pt 6), 531-544. DOI: 10.1107/S2059798318006551.